Predicting low-impedance interfaces for solid-state batteries

Michael W. Swift[a,b], Harsh Jagad[c], Jiyun Park[a,c], Yu Qie[a], Yuqin Wu[a,c], Yue Qi[a,c]

[a] *Department of Chemical Engineering and Materials Science, Michigan State University, East Lansing, MI, 48824-1226, USA*
[b] *Center for Computational Materials Science, US Naval Research Laboratory, Washington, DC, 20375, USA*
[c] *School of Engineering, Brown University, Providence, RI, 02912, USA*

Abstract

All-solid-state batteries are an exciting technology for increased safety and energy density compared to traditional lithium-ion cells. Recently, we developed a theory of mapping inner potentials and thermodynamic driving forces specific to the solid-state batteries, allowing prediction of the "intrinsic" interfacial lithium barriers. This potential mapping methodology, based purely on calculated bulk and surface properties, enabled fast screening of a variety of advanced solid electrolyte materials as well as a selection of cutting-edge high-voltage cathode materials, predicting properties of 48 distinct battery configurations. A number of cathode/electrolyte pairs are identified which have low "intrinsic" barriers to both the charge and discharge process at all states of charge, suggesting that they will most benefit from engineering efforts to reduce extrinsic interfacial impedance. These predictions agree well with available experimental measurements, which form only a subset of the predicted interfaces. Thus, this interface potential model will accelerate the design process from emerging materials to all-solid-state battery devices.

Keywords: solid-state batteries, interfacial impedance, battery modeling, electrode-electrolyte interface, potential maps, density functional theory

1. Introduction

Lithium-ion batteries have revolutionized electrical energy storage technology, ranging from portable electronics, electric vehicles, aerospace products, to grid storage, providing an integrated solution with renewable energy sources. [1] Recently, all-solid-state batteries (ASSBs) attracted enormous attention as one promising technology for safe and high-energy-density batteries, as ASSBs not only allow the deployment of high-energy-density lithium-metal anodes, [2] but also solve the thermal runaway problem caused by flammable liquid electrolytes. With the increasing number of solid-electrolyte (SE) materials with high ionic conductivity [3] and the shrinking thickness of the SE for higher energy density, Li-ion diffusion within the solid electrolyte is no longer the bottleneck. Instead, high resistance at the interface becomes the rate-limiting step. [4, 5, 6] Subsequently, the reduction in performance of many ASSBs, including the poor power performance, low Coulombic efficiency, and short cycling life, can all be traced to the high interface resistances. [6]

Many factors can contribute to the high interface resistance in ASSB, including the lack of intimate contact between the electrodes and the SE, [7, 8] the presence of decomposed SE interphases at thermodynamically unstable SE/electrode interfaces, [9, 10, 11, 12, 13] and space-charge-layer formation. [14, 15, 16] These factors are interconnected. For example, the large volume change due to SE decomposition causes interface cracking and loss of contact [17] and the formation of the interphase layer will create an additional space charge layer between the electrode and the SE. [18] The formation of the interface/interphase is a complex process and highly depends on the fabrication temperature and/or synthesis route [19, 20] of the ASSBs. Due to these complexities, the reported interface resistance may differ by orders of magnitude even within the same materials system. [21, 22, 23, 24, 25]

The inability to delineate the various factors that contribute to interface impedance severely hinders the progress of interface engineering and all-solid-state battery design. A clear picture of the "intrinsic" resistance for a given pair of electrode and solid-electrolyte materials is needed for comparing and designing ASSB systems. Based on these predictions, improved ASSB de-

Email address: YueQi@brown.edu (Yue Qi)

signs should use materials whose interfaces have low intrinsic impedances, so that mitigation of extrinsic impedances will result in a battery with high performance overall.

Intrinsic impedances would arise even at a pristine interface with perfect contact and without interphase formation. Electrons (or holes) and ions will redistribute at heterogeneous interfaces, causing an intrinsic electrostatic potential jump. The electronic part arises from physics analogous to the well-understood band bending in semiconductor devices, [26], while the ionic part is similar to the "space-charge-layer" in ionic conductors. [27, 18] The electrostatic fields caused by the electrostatic potential jump at the interface were suggested as possible barriers to lithium migration across interfaces. [28, 29, 30, 31] Previously, Swift and Qi demonstrated a first-principles-informed theoretical framework to predict the interfacial electrostatic potential jump [27] and space-charge layers [18] within solid-state batteries. The modeling results agreed well with Kelvin probe force microscopy measurements [32], which proposed that interfacial electric fields arising from electronic band alignments may lie behind much of the reported interfacial resistance. This intrinsic interface property does not scale with the contact area. The intrinsic interfacial resistance and the contact area, which can be controlled by the battery architecture and stack pressure ("extrinsic" interface properties) and modeled with continuum contact mechanics, jointly describe the macroscopic interface resistance. Furthermore, the interphase layer can be explicitly included in the battery systems as electrode/interphase/SE and modeled using these techniques as demonstrated before [18] for more complex interfaces.

In this work, we expand the interface potential map model [27] to a variety of solid-state battery materials classes, as illustrated in Fig 1. As the model is based on bulk, surface, and defect properties calculated from first principles by density functional theory (DFT), it is predictive rather than empirical. The model is built on the thermodynamic driving forces acting on electrons and ions, so the results do not rely on expensive explicit interface calculations at the DFT level, [33, 34, 35, 36] enabling rapid screening of battery systems. Here we predict potential maps in 20 ASSB systems assembled from Li-metal anode, four solid electrolyte materials, and five cathode materials. Taking into account changes in the cathode with state of charge (SOC), there are 12 SE/cathode interfaces, for a total of 48 distinct ASSB configurations in the dictionary. This can easily be expanded to include more materials by simply calculating appropriate bulk, surface, and defect properties using

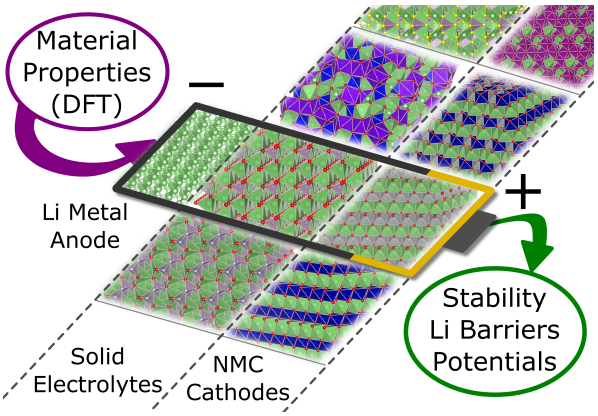

Figure 1: Graphic illustrating the dictionary of solid-state battery potential maps. The general first-principles-informed model can predict potentials and lithium barriers in an all-solid-state battery with a lithium metal anode, any solid electrolyte material, and any cathode material. In this work, we choose sets of solid electrolyte and cathode materials, and present the results for each material pair. Materials shown here are among those included in the dictionary: metal anode Li; solid electrolytes Li_2PO_2N, Li_3PO_4, $Li_7La_3Zr_2O_{12}$, and Li_3PS_4; layered cathodes $LiCoO_2$, $LiNiO_2$, and Li_2NiCoO_4, and spinel cathode $LiMn_2O_4$.

DFT. Comparing with existing experimental ASSB literature, we show that measured interfacial resistances are indeed correlated with our predicted interfacial electrostatic potential jump. Furthermore, this framework predicts that the resistance at a given interface may depend on the battery SOC, explaining results from various experimental groups that might initially appear contradictory. For the same material class, some groups present a high value of resistance [14, 25, 22], and some reported a low value of resistance [20, 37, 38] a difference which may result from measurements taken at different SOC.

The results not only move us towards a more intrinsic picture of the nature of the interfacial resistance, but also provide an ASSB system design tool with a reference repository of materials behavior for future experimental work.

2. Theory and Methods

Potential maps are calculated following the methodology of Ref. 27. The model starts from the assumption of open-circuit equilibrium: the SE blocks the flow of electrons, but lithium ions are free to move throughout the battery until they reach equilibrium. In open-circuit equilibrium, the electrochemical potential of lithium ions, $\tilde{\mu}_{Li^+}$, reaches a constant. Since only electrochemical potential *differences* are physically meaningful, we

define this constant value to be $\tilde{\mu}_{\mathrm{Li}^+} = 0$. Therefore, the atomic chemical potential of lithium, μ_{Li}, is given by

$$\mu_{\mathrm{Li}} = \tilde{\mu}_{\mathrm{Li}^+} + \tilde{\mu}_{e^-} = \tilde{\mu}_{e^-} \tag{1}$$

where $\tilde{\mu}_{e^-}$ is the electrochemical potential of electrons. These chemical potentials may be related to the open-circuit voltage (OCV) through

$$\mathrm{OCV} = \frac{1}{e}\left(\mu^a_{\mathrm{Li}} - \mu^c_{\mathrm{Li}}\right) = \frac{1}{e}\left(\tilde{\mu}^a_{e^-} - \tilde{\mu}^c_{e^-}\right) , \tag{2}$$

where superscripts a and c denote the anode and cathode respectively. The OCV for a cell with a given cathode material $\mathrm{Li}_\alpha\mathrm{X}$ against lithium metal is given by the average voltage of the lithiation reaction [27, 39]

$$\mathrm{Li}_\beta\mathrm{X} + (\alpha - \beta)\mathrm{Li} \rightarrow \mathrm{Li}_\alpha\mathrm{X}$$

$$\mathrm{OCV} = -\frac{E[\mathrm{Li}_\alpha\mathrm{X}] - E[\mathrm{Li}_\beta\mathrm{X}] - (\alpha-\beta)E[\mathrm{Li}]}{(\alpha-\beta)e} , \tag{3}$$

where $E[]$ denotes the DFT total energy of the compound in brackets, α is the lithium content of the cathode material, and β is the lithium content of the reference phase. For example, the OCV of $\mathrm{LiCoO_2}$ is the voltage of the reaction $\mathrm{CoO_2} + \mathrm{Li} \rightarrow \mathrm{LiCoO_2}$: in this case $\alpha = 1, \beta = 0$, and $\mathrm{X} = \mathrm{CoO_2}$. Further details of the model and the first-principles computational methodology may be found in the Supplementary Information.

It is clear that μ_{Li} must change from its value in the anode to its value in the cathode across the battery. This potential drop occurs through some mixture of the interfaces and the bulk of the electrolyte; the extent to which μ_{Li} gradients exist in the electrolyte is an open problem. [27]

In the solid electrolyte, allowed values are constrained by the formation of alternative phases. The range of μ_{Li} values for which a given solid electrolyte material is stable is its electrochemical window. In this work, we assume the maximum μ_{Li} change that is allowed by the electrochemical window takes place within the bulk of the solid electrolyte. The remainder occurs at the interfaces. This represents the smallest possible change in μ_{Li} at each interface, and has previously been called the "minimum interface" assumption. [27]

In order to determine the position of the electronic bands, the position of the Fermi level within the material's band structure must be determined. This is accomplished by the calculation of charged point defect formation energies. The equilibrium Fermi level E_F (which in our convention is referenced to the VBM of the material) is determined by charge balance among competing point defects. [40, 41, 27] Point defect calculations are partially automated using PyCDT [42] and pymatgen [43] and the results are shown in Figures S-1 to S-4 in the Supporting Information I. The position of the SE VBM relative to the anode Fermi level thus depends on μ_{Li} through

$$\mathrm{VBM} = \mu_{\mathrm{Li}} - E_F(\mu_{\mathrm{Li}}) \tag{4}$$

The ionization potential IP is the position of the VBM below the local vacuum, and is calculated for the lowest-energy termination of each given material using a slab methodology, partially automated using pymatgen. [43] Referencing $\mu^a_{\mathrm{Li}} = 0$ and letting ψ^a be the work function of the anode, it can be shown [27] that

$$\tilde{\mu}_{\mathrm{Li}^+} = \mu_{\mathrm{Li}} - (E_F - IP + \psi^a - e\phi) = 0 . \tag{5}$$

This equation may be solved for ϕ to get the electrostatic potential profile.

In Fig 2, all bands are aligned to the local vacuum level by their ionization potential (IP), calculated using DFT from a slab model with the lowest-energy surface termination. [27] Note that the IP is equal to the work function in metals (such as Li), but for the solid electrolytes the two quantities are distinct. The IP is the energy difference between the VBM and the vacuum, whereas the work function is the energy difference between the Fermi level (E_F) and the vacuum. We treat the IP as constant, whereas the position of the Fermi level within the gap (and thus the work function) depends sensitively on growth and processing conditions and possibly on the state of charge of the battery. The cathode materials investigated here show heavily p-type character, with the Fermi level near the top of the valence band and IP very close to the work function.

All the solid electrolyte materials are ionic conductors and electronic insulators, with band gaps larger than 2 eV. The band gap in cathode materials can vary with the state of charge. Layered $\mathrm{LiCoO_2}$ (LCO) becomes more electronically conducting with less Li or higher SOC, while $\mathrm{LiNiO_2}$ (LNO) and $\mathrm{Li_2(NiCo)O_4}$ (LNCO) do not show such strong SOC dependence of the band gap. Interestingly, the band gaps of spinel $\mathrm{LiMn_2O_4}$ (LMO) and $\mathrm{Li_x(Ni_{0.5}Mn_{1.5})O_4}$ (LNMO) show different SOC dependence. Although it is known that semi-local functionals like PBE underestimate the the band gap, we have found that in lithium conductors the ionization potential tends to be fairly accurate, with most of the gap underestimation coming from an under-prediction of the conduction band energies. Since we use the VBM as the energy reference and primarily deal with solid electrolytes with Fermi levels far from the conduction-band

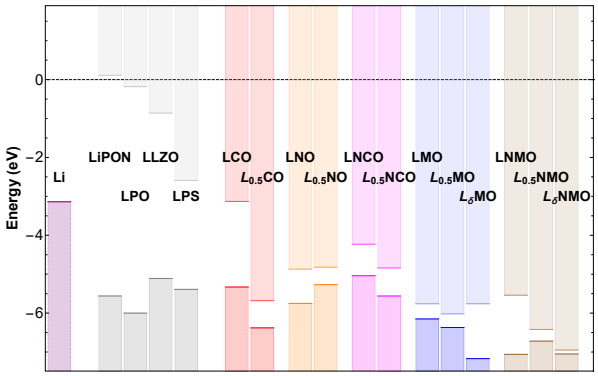

Figure 2: The vacuum-aligned positions of electronic bands in lithium metal anode; LiPON (purple), LPO, LLZO, LPS solid electrolytes (gray) ; LCO (red), LNO (orange) and LNCO (magenta), LMO (blue), LNMO (brown) cathodes. Occupied bands (VBM) are shown in darker colours and unoccupied bands (CBM) are shown in lighter colours

minimum (CBM), PBE results are sufficient for our purposes. If needed, a "scissor shift" based on a higher level of theory could easily be used to adjust the conduction and valence band energies.

3. Results and Discussion

3.1. Electrode and Solid Electrolyte Materials

There are wide variety of lithium-ion solid electrolytes under exploration in the literature. We include four in the present study, chosen to represent different classes of solid electrolyte chemistry. Fig 2 shows the bands of the individual electrode and electrolyte materials investigated in this paper and their detailed structures are shown in Table S-1 in the Supporting Information I.

Lithium phosphorus oxynitride (LiPON) is one of the most successful solid electrolyte materials due to its resistance to lithium dendrites [44, 45]. As a proxy for amorphous LiPON, we use the crystalline analogue Li_2PO_2N [46], which is similar to ALD-grown LiPON. [47] We also study Li_3PO_4 (LPO), which when doped with nitrogen is a good proxy for PVD-grown LiPON [48], and which is also a promising ionic conductor in its own right, exhibiting low interfacial resistance. The third material we include is Li_3PS_4, which represents a broad class of sulfur-based solid electrolytes. These materials show promising performance, but must be coated at the electrode interfaces due to their narrow electrochemical stability window. [49] Finally, we include $Li_7La_3Zr_2O_{12}$ (LLZO), a "superionic conductor" with fast performance and good electrochemical stability [50, 51, 52], but whose applications are so far limited due to dendrite growth [53].

Five cathode materials were investigated. For layered intercalation compounds, $LiCoO_2$, $LiNiO_2$, and $Li_2(NiCo)O_4$ were considered. LCO is the most commonly used cathode material for lithium-ion batteries. [54, 55] $LiNiO_2$ was investigated as the parent structure for high Ni content layered cathode materials, [56, 57, 58, 59] including layered compounds with ordered Ni and Co distributions in the transition-metal layer such as $Li_2(NiCo)O_4$ [60, 61] for high power applications. Spinel $LiMn_2O_4$ cathode materials were also included due to their structural stability and very small volume change during cycling. [24, 62] Finally, we selected the high-voltage spinel cathode $Li_x(Ni_{0.5}Mn_{1.5})O_4$, not only because of the technological promise of high-voltage batteries enabled by SE [21, 63] but also in order to illustrate the impact of the cathode voltage on the interfacial resistance. Since material properties vary with Li concentration, we have modeled a fully lithiated cathode (SOC 0%) and a half lithiated state. For the layered materials, we have assumed that half lithiation represents the fully charged state (SOC 100%), since further delithiation often leads to irreversible phase transformations. However, spinel materials can reach a deep delithiation state without lattice collapsing, so we also considered the delithiated limit for the spinels, which we label L_{δ}MO and L_{δ}MNO (overcharged, or SOC +). Advanced high-Ni layered cathodes have also demonstrated the ability to cycle reversibly up to 80% delithiation [64, 65], but accurate modeling of deep delithiation in layered materials remains a challenge.

3.2. Potential change at the Li/solid-electrolyte interface

The change in electrostatic potential at the Li/SE interface (see Figure 3) is given by

$$\Delta\phi^a = \phi_{\mathrm{SE;Li}} - \phi_{\mathrm{Li}} \,, \tag{6}$$

where ϕ_{Li} is the electrostatic potential in the Li and $\phi_{\mathrm{SE;Li}}$ is the electrostatic potential in the SE at the closest point to Li within its stability window. According to the values shown in Figure 3, $\Delta\phi^a$ is +0.28, +1.42, +1.62, and +1.67 eV for Li/LiPON, Li/LPO, Li/LLZO, and Li/LPS interfaces, respectively. This potential discontinuity causes some Li ions to transfer from the Li-metal into the solid electrolyte during interface formation, creating the space-charge layer. Electrons and holes may transfer as well, especially at the Li/LPS interface, but given the large band gap of the SE and the separation between the Li Fermi level and the SE band edges, ion transfer is expected to dominate at this interface.

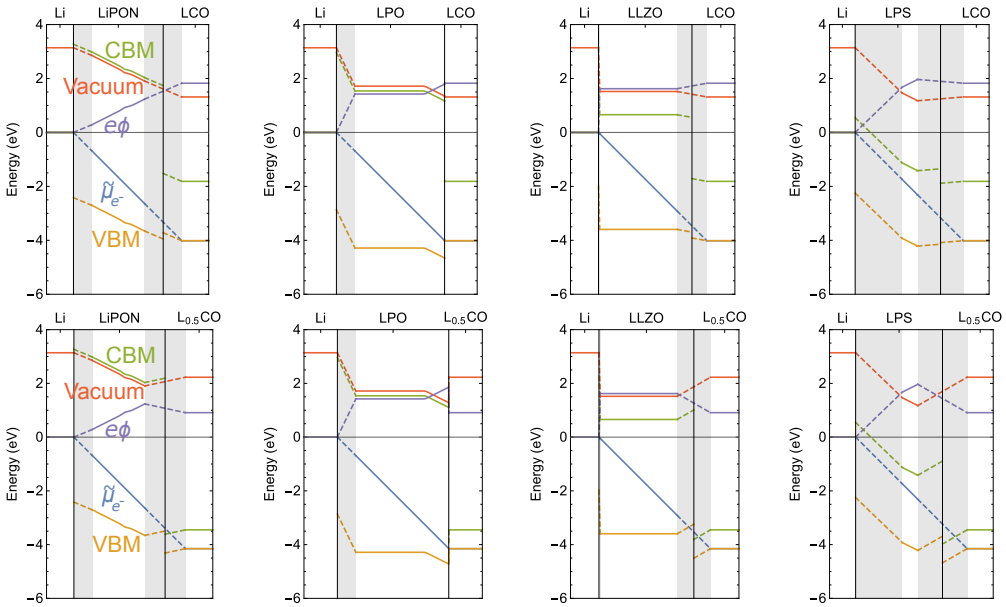

Figure 3: Comparison of potential maps for LiPON, LPO, LLZO and LPS Solid electrolytes with lithium metal anode with a LCO cathode. The two rows show two different scenarios, top row shows the case for a fully discharged state and bottom row shows for fully charged state

Depending on the electrochemical process being considered, $\Delta\phi^a$ may or may not act as a barrier. During the discharge process, the direction of Li-ion transfer is from the lithium metal into the solid electrolyte. In this case, a positive $\Delta\phi^a$ indicates a barrier to lithium migration, and a negative $\Delta\phi^a$ would not represent a barrier. On the other hand, during charging, the direction of lithium-ion transfer reverses. Therefore a positive $\Delta\phi^a$ does not act as a barrier during charging, while a negative $\Delta\phi^a$ would. For each Li/SE interface, the barrier for Li^+ migration is positive, meaning that work must be done on the lithium-ion by the external electric field to overcome this barrier when transferring more ions from the anode to the SE during discharge. During charging, however, the lithium ions transfer from the SE into the anode almost freely.

Depending on the band-alignment of lithium and the solid electrolyte material, certain predictions regarding the thermodynamic stability of the interface may be made. Lithium metal is one of the most highly reductive materials available since it readily gives away the unpaired $2s^1$ electrons. Decomposition *via* electrochemical reduction is one possible mechanism behind interfacial instability. For LiPON, LPO and LLZO, the CBM lies well above the lithium Fermi level, and hence the electrons from lithium do not readily reduce the electrolytes. However, for LPS, the absolute position of the CBM is close to the lithium Fermi level (Figure 2), and the CBM moves below the lithium Fermi level once interfacial band bending has been included (Figure 3). Hence LPS is readily reduced by electrons from Li, leading to further decomposition. This is corroborated by explicit interface modeling [49] and experimental results which report an unstable reactive interface between lithium metal and LPS. [71] The agreement with experiments also indicates the importance of using the potential map of a full cell to align the band positions instead of comparing the electronic energies of zero-charged individual materials.

The band alignments also explain tendency of lithium dendrite formation along the anode-electrolyte interface during the charging process. During charging, lithium ions migrate into the anode from the electrolyte. If the Fermi level of lithium is lower than the CBM of the electrolyte, lithium ions can transfer into the anode and gain one electron and hence, dendritic growth does not take place. For LiPON, the gap between lithium Fermi level and LiPON CBM is around 3 eV and hence Li/LiPON interface is generally reported to be dendrite free. [72] For Li/LLZO, the difference in the energy levels between the lithium metal Fermi level and electrolyte CBM is less than 1 eV, and hence, electrons from lithium metal are able to tunnel through the barrier during charging. This phenomenon has been reported widely in literature especially at higher current densities which increases the electron jumping frequency. [73] Furthermore, internal defects such as pore surfaces and grain boundaries will have a lower conduction band or

Table 1: Cathode/SE interface potential change $\Delta\phi^c$, as given by Eq. (7). Values are shown for various interfaces in the discharged (SOC 0%), charged (SOC 100%), and overcharged (SOC +) state. Positive $\Delta\phi^c$ is a barrier to discharging, while negative $\Delta\phi^c$ is a barrier to charging. Experiments measuring the interface resistance for the given cathode/SE pair at the specific SOC are cited for comparison. The experimental resistance data (in Ω cm^2) was categorized as very low < 10; 10 < low < 100; 100 < medium < 500; 500 < high < 1000; very high > 1000. When different processing conditions were considered, the lowest values are taken. If the electrode was coated, it is specified, otherwise values are for bare uncoated electrode. The SOC of the experimental cells is indicated in parentheses if explicitly mentioned in the reference, otherwise NA is used.

Interface	SOC	$\Delta\phi^c$ (V)	Reference in literature
LCO-LiPON	0%	+0.61	Considered-High (NA)
	100%	−0.35	[14]
LCO-LPO	0%	+0.07	Very low - (100%) [20],
	100%	−0.96	(100%) [66], (0%) [21]
LCO-LLZO	0%	+0.19	Considered-High (NA)
	100%	−0.72	[13]
LCO-LPS	0%	−0.10	High (NA) [67] ; Medium (0%)
	100%	−1.01	[68]; Low at LPS/ LCO/LNMO (0%) [69]
LNO-LiPON	0%	+0.30	-
	100%	+0.79	
LNO-LPO	0%	−0.32	-
	100%	+0.16	
LNO-LLZO	0%	−0.09	-
	100%	+0.41	
LNO-LPS	0%	−0.39	Considered-High, reduced by
	100%	+0.09	LCO (0%) [69]
LNCO-LiPON	0%	+1.06	-
	100%	+0.69	
LNCO-LPO	0%	+0.42	-
	100%	+0.06	
LNCO-LLZO	0%	+0.67	-
	100%	+0.31	
LNCO-LPS	0%	+0.36	Considered-High,
	100%	+0.01	reduced by coatings (0%) [69], (0%) [59]
LMO-LiPON	0%	−0.24	Very High (0%) [25],
	100%	−0.49	Considered-High (NA) [24]
	+	−1.35	
LMO-LPO	0%	−0.63	
	100%	−1.00	-
	+	−1.85	
LMO-LLZO	0%	−0.64	Medium (NA) [70]
	100%	−0.87	Low-Medium
	+	−2.62	(0,100%) [37]
LMO-LPS	0%	−0.92	
	100%	−1.17	-
	+	−2.03	
LNMO-LiPON	0%	+0.07	Very High (~90%) [22],
	100%	+0.80	Medium (0%) [21]
LNMO-LPO	0%	−0.56	Very Low (0,100%)
	100%	+0.17	[38]
LNMO-LLZO	0%	−0.34	Beneficial Interlayer
	100%	+0.41	(NA) [70]; Low increases with cycling
LNMO-LPS	0%	−0.61	(0,100%) [37]
	100%	+0.11	-

even trap electrons, inducing dendrite growth. [74, 75] For LPS, during charging, the barrier is negative and hence electrons from the lithium metal readily pair with the incoming lithium ions and precipitate at the interface [71, 72]

A related factor is the electrochemical stability of the SE, calculated using established methodology [9] based on Materials Project phase diagram analysis [76, 77]. The stability windows of the SE materials (in volts versus Li metal) are (0.68, 2.64) for LiPON, (0.69, 4.21) for LPO, (0.00, 2.91) for LLZO, and (1.74, 2.32) for LPS. Gray shaded regions in Figure 3 show areas where μ_{Li} is outside the stability window of the SE: these potential drops must occur at the interface.

3.3. Potentials in the solid electrolyte: flat or sloped?

Figure 3 shows the potential map for four solid-state batteries consisting of four different solid electrolytes connecting Li and LCO electrodes. In the potential map plots, μ_{Li} (blue lines in Figure 3) in the solid electrolyte was assumed to vary linearly from the anode to the cathode. For visualization purposes, μ_{Li} is plotted with the same slope in different battery systems. While the slope of the electrochemical potential of electrons in an actual device will depend on many factors including device geometry, the choice of an equal slope in all the plots highlights the information contained in the plots. Firstly, the width of the plot corresponds to the OCV between Li metal and the cathode material, not the geometry of a device. Secondly, since regions with μ_{Li} values which are outside the electrochemical window of the electrolyte are shaded in gray, the width of the shaded regions indicates the instability or reactivity of the interface. It can be seen that LLZO is the most stable against Li-metal, and LPO is the most stable against the LCO, while LPS has the narrowest electrochemical stability window. The potential drop in this shaded region must occur at the interface/interlayer.

A noticeable difference between the materials is whether the VBM, CBM, and $e\phi$ (corresponding to the orange, green and purple lines respectively in Fig 3) are sloped (in LiPON and LPS) or flat (in LLZO and LPO when $-\mu_{\mathrm{Li}}$ is lower than 3 eV). This is determined by the defect chemistry, which is very different among the studied SE materials. As shown in Fig 4, the dominant lithium defect in LiPON switches from lithium interstitial to lithium vacancy as voltage increases. These defects are balanced by the substitution of N on O or O or N. LPO and LLZO show lithium vacancies and interstitials in balance with constant concentration to approximately 3 V, at which point LLZO becomes unstable whereas LPO develops a significant lithium vacancy

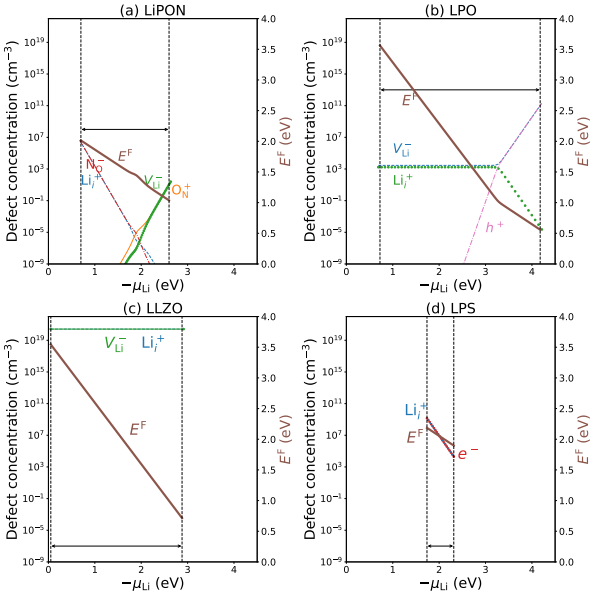

Figure 4: Concentrations of point defects, electrons, and holes that determine the Fermi level in the various solid electrolyte materials, plotted as a function of $-\mu_{\mathrm{Li}}$ (or voltage). (a) LiPON, (b) LPO, (c) LLZO, and (d) LPS. Fermi level as a function of voltage in solid electrolyte materials based on intrinsic defects is shown on the secondary axis and marked in brown colour. The black arrow (between the dotted lines) represents the stable electrochemical window for the electrolytes. The slopes of -1 in LLZO and LPO below 3V result from the balance between lithium vacancies and interstitials whose formation energies both depend directly on μ_{Li}. The slopes of $-1/2$ in LiPON, LPS, and LPO above 3V result from the balance between a lithium defect and a non-lithium charged species.

concentration balanced by an increasing hole concentration. In LPS a relative lack of favorable negatively charged defects means that lithium interstitials are balanced by electrons throughout its narrow stability window.

The differences in defect chemistry also affect the Fermi level dependence on μ_{Li}, as shown in Figure 4. Depending on the defects which determine the Fermi level, the slope of this dependence can vary. In the case of balance between a lithium interstitial and vacancy, the formation energies depend oppositely on μ_{Li}, so the Fermi level at which they cross has a slope of -1 in the figure. The changes in Fermi level and lithium chemical potential thus cancel out and the VBM and $e\phi$ remain constant, according to Equations 4 and 5, respectively. This is the case for LLZO and LPO below approximately 3 V. In the case of a Fermi level determined by a lithium defect and a non-lithium defect, the slope is $-1/2$. This is the case for LPS, LiPON, and LPO above approximately 3 V.

While many continuum-level of models have assumed that Li-ion concentration is a constant in the solid electrolyte and therefore the electrostatic potential must be a constant, [78] our theoretical framework considers the electrochemical potential of Li ions to be a constant at the OCV equilibrium. The electrostatic potential is an outcome of the chemical potential change in the solid electrolyte and the defect chemistry. As most previous continuum models only considered charge balance between positive ions and negative ions without taking the electronic structure of the solid electrolytes into account, these assumptions limit the applicability of previous models to special cases, such as LPO or LLZO. Our predictive model works self-consistently across all the possible cases.

3.4. Potential change at the cathode/solid-electrolyte interface

We consider the effect of forming interfaces between the electrolytes discussed earlier with a broad range of cathode materials at different SOC. The potential jump at the cathode/SE interface is defined analogously to Eq. (6):

$$\Delta\phi^c = \phi_{\mathrm{cathode}} - \phi_{\mathrm{SE;cathode}}\ , \tag{7}$$

where ϕ_{cathode} is the electrostatic potential in the cathode and $\phi_{\mathrm{SE;cathode}}$ is the electrostatic potential in the SE at the closest point to the cathode within its stability window. Similarly to $\Delta\phi^a$, a positive $\Delta\phi^c$ represents a barrier for discharging while a negative value becomes a barrier for Li transport across the interface during charging. The value and the sign of the barrier depend on the

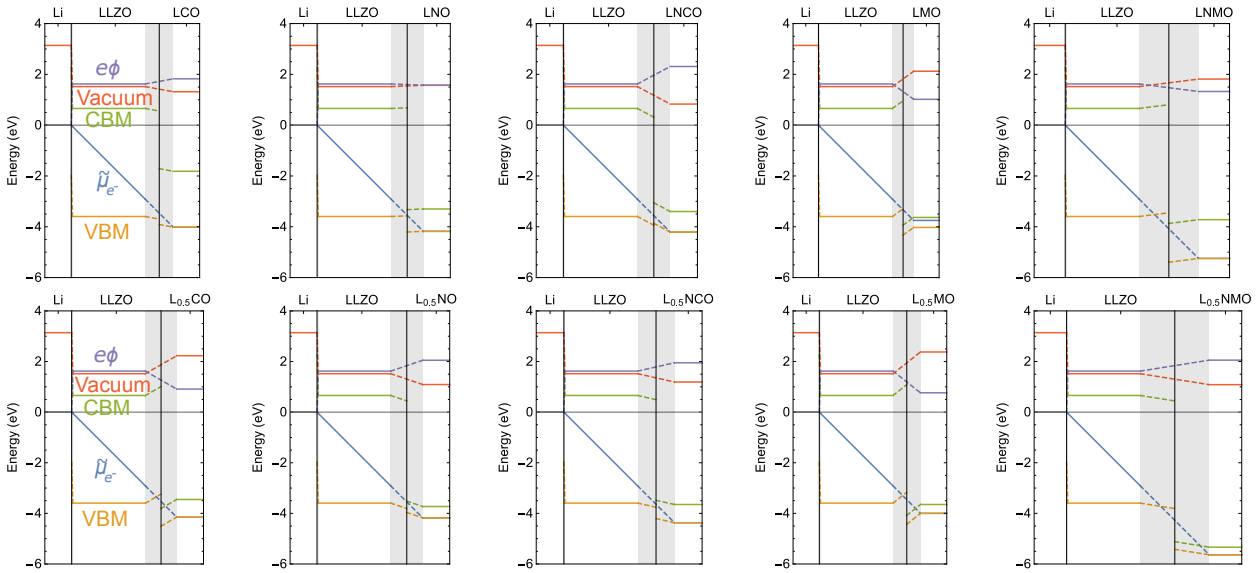

Figure 5: Comparison of potential maps showing a lithium metal anode and LLZO solid electrolyte with different cathodes: LCO, LNO, LNCO, LMO, and LNMO. Again, the top row shows the fully discharged state while the bottom row shows the fully charged state.

cathode materials and their state of charge (SOC). Fig 5 showed Li/LLZO/cathode potential maps for five different cathode materials at two states of charge (other ASSBs are shown in the Supplementary Information II) and the values of $\Delta\phi^c$ for all SE/cathode material pairs and SOC are given in Table 1. These results provide relevant insights into the cathode-electrolyte interactions and highlight the changes in the thermodynamic landscape that occur during the electrochemical process between the cathode and the electrolyte.

In several systems, the potential barrier has opposite signs in the charged and discharged state. For example, the LCO/LiPON, LCO/LPO, LCO/LLZO systems (Figure 3) exhibit positive barrier for lithium-ion migration at the electrolyte/cathode interface at the beginning of the charge process, but by the end of the charge process, the barrier becomes negative. On the other hand, LNCO/LLZO shows positive barrier at both SOCs and LMO/LLZO shows negative barriers at both SOCs (Figure 5). In general, all interfaces shows SOC-dependent interfacial barriers, therefore it will be hard to generalize observations from both modeling and experiments.

Table 1 also listed experimental observations for the same interfaces. The predicted potential change at the interface cannot be directly mapped to the interface resistance, but can still be quantitatively related to experimental observations. It is important to note that the potential barrier creates direction-dependent resistance (i.e., different in charge vs. discharge) for Li ion transport. In experiments, impedance is often measured by Electrochemical Impedance Spectroscopy (EIS), which uses small alternating currents as input, measures the voltage drop as output, and infers the impedance of the systems using an effective circuit model. Since EIS uses alternating current (AC), it measures the barrier in the rate-limiting direction and thus can be related to the absolute values of the potential drops $|\Delta\phi|$. EIS cannot capture the directional dependence represented by the signs of $\Delta\phi$. [32] Techniques such as Galvanostatic Intermittent Titration Technique [79] and load charge/discharge need to be used in conjunction with EIS to develop a complete picture of the direction-dependent resistance. Interpretation of EIS is additionally complicated by the fact that it is difficult to resolve distinct electrochemical processes if they occur at similar frequencies.

It is interesting to note that the computed $|\Delta\phi^a|$ and $|\Delta\phi^c|$ can both reach a high value (above 1 eV), however the reported interfacial resistance at Li/SE interface is often one or two orders of magnitude lower than the Cathode/SE interface, [80, 66] suggesting interface contact may be a main contributor. Therefore, if interface contact and other extrinsic impedances can be mitigated, the remaining intrinsic barriers at low-barrier cathode/SE interfaces ($|\Delta\phi^c| \sim$ 0.3-0.4 eV) should correlate to very small impedances and good performance.

Interfacial reactions can also create additional phases which may impede Li-ion transport. The width of the gray area in Figs. 3 and 5 is proportional to the potential drop that needs to occur for stable battery op-

eration. With increasing voltage of the cathode materials (Fig. 5), the necessary potential drop becomes larger. For example, in the case of the high voltage LNMO/LLZO interface, the gray region increases in width with increasing delithiation. The defect chemistry of the interfacial region also influences the direction-dependent impedance due to the space-charge layer. The present model gives a minimum value for the potential change, but with a non-ideal interlayer, the resulting impedance can be more severe.[18] Since the interface potential drop is inevitable with or without a coating interlayer, application of a coating layer can in principle stabilize the interface. On the other hand, if the interlayer is too thick or has a very low ionic conductivity, Li^+ transport through the interlayer could become the bottleneck, dominating the contribution of $\Delta\phi$ to the interfacial impedance. If the thickness of the coating layer is controlled, its effect on Li^+ transport will be minimized and it will not introduce additional barriers to the intrinsic electrostatic barrier.[18]

Among all the interfaces investigated here, "barrierless" interfaces ($|\Delta\phi^c| < 0.1$ eV) include fully discharged LCO/LPS, LNO/LLZO, LNMO/LiPON and fully discharged LNO/LPS LNCO/LPO, LNCO/LPO, LNCO/LPS interfaces. There are a number of interfaces with low $|\Delta\phi^c|$ on the order of 0.3-0.4 eV over the entire SOC range, including LNO/LPO, LNO/LLZO, LNO/LPS, LNCO/LPO, LNCO/LPS, and LNMO/LLZO interfaces. The scattered experimental data in general agree with the computed trends. For example, the interfaces reported very low resistance (LCO/LPO), LNMO/LPO) do have low barriers at the interface at certain state of charge. For interface resistance that can be reduced by stabilized interlayers [69], such as LNCO/LPS or LNO/LPS, we predict that at least one of their intrinsic barriers is low. Adding an LCO interlayer can therefore further reduce the interface resistance, [69] especially if the LCO is fully lithiated on the surface, because the LCO/LPS interface barrier is also rather small. In contrast, the predicted interface barrier at LMO/LPS is high in all three SOC, indicating it may be harder to achieve low resistance at this interface.

4. Conclusions

All-solid-state batteries offer a promising future for lithium-ion-based energy storage, since they allow incorporation of lithium metal anodes and solve the flammability problem of liquid or gel electrolytes. However, current all-solid-state batteries suffer from obstacles including relatively high impedance.

In this work, we employed a first-principles-informed thermodynamic model to quantify the electrochemical potentials driving lithium ion movement in all-solid-state batteries, and connected this model to interfacial stability and interfacial resistance. By modeling a lithium metal anode with four solid electrolytes (LiPON, LPO, LLZO, and LPS) and five cathode materials (LCO, LNO, LMO, LNMO and LNCO), we have built a "dictionary" of predicted intrinsic interface potential barriers. We address the complex debates around the nature of the potential barrier that is flat (or constant barrier) or sloped (or variable barrier) across the electrolyte. The nature of this barrier depends on the slope of the intrinsic defect concentration. We also address the existence (or lack) of a barrier at a given interface during the charge and discharge processes.

Based on these results, we have identified a number of promising cathode/solid-electrolyte pairs which exhibit low intrinsic barriers for both lithium transfer directions across all states of charge. These include LNO/LPO, LNO/LLZO, LNO/LPS, LNCO/LPO, LNCO/LPS, and LNMO/LLZO. Reducing extrinsic impedances by optimizing interface stability and increasing contact area will be engineering strategies to reduce macroscopic interface resistance. If interfacial challenges such as high-impedance interlayers or extrinsic sources of impedance can be avoided or mitigated in these cathode/solid-electrolyte pairs, only the small intrinsic impedances from the electrostatic potential will remain, allowing for high-performance ASSBs. If this methodology is extended to include promising new ASSB materials as they are proposed, it will identify the material pairs with reduced intrinsic impedance, thereby guiding experiments and explaining observations in both established and emerging all-solid-state lithium-ion batteries.

5. Author Contributions

Conceptualization: M.W.S. and Y.Qi; Data curation: M.W.S. and H.J.; Formal Analysis: M.W.S. and Y.Qi; Funding acquisition: Y.Qi; Investigation: M.W.S., H.J., J.P., Y.Qie, and Y.W.; Methodology: M.W.S. and Y.Qi; Project administration: M.W.S. and Y.Qi; Software: M.W.S.; Supervision: M.W.S. and Y.Qi; Validation: M.W.S. and H.J.; Visualization: M.W.S., H.J., J.P., Y.Qie, and Y.W.; Writing – original draft: M.W.S and Y.Qi; Writing – review & editing: M.W.S, H.J., and Y.Qi

6. Acknowledgements

M. W. S. acknowledges support from the Naval Research Laboratory Postdoctoral Fellowship through the American Society for Engineering Education. H. J., J. P., Y. W., and Y. Qi acknowledge the support from the National Science Foundation under Grants No. DMR-2054441. Y. Qie was supported by a scholarship from Peking University to conduct research at MSU.

7. Data availability

The raw/processed data required to reproduce these findings cannot be shared at this time due to technical or time limitations. The raw data (DFT calculations) will be collected and uploaded to the NOMAD repository and the processed data will be uploaded to Mendeley Data.

References

[1] A. Manthiram, An outlook on lithium ion battery technology, ACS Cent. Sci. 3 (10) (2017) 1063–1069. doi:10.1021/acscentsci.7b00288.

[2] P. Albertus, S. Babinec, S. Litzelman, A. Newman, Status and challenges in enabling the lithium metal electrode for high-energy and low-cost rechargeable batteries, Nat. Energy 3 (1) (2018) 16–21. doi:10.1038/s41560-017-0047-2.

[3] Z. Zhang, Y. Shao, B. Lotsch, Y.-S. Hu, H. Li, J. Janek, L. F. Nazar, C.-W. Nan, J. Maier, M. Armand, L. Chen, New horizons for inorganic solid state ion conductors, Energy Environ. Sci. 11 (2018) 1945–1976. doi:10.1039/C8EE01053F.

[4] A. C. Luntz, J. Voss, K. Reuter, Interfacial challenges in solid-state Li ion batteries, J. Phys. Chem. Lett. 6 (22) (2015) 4599–4604. doi:10.1021/acs.jpclett.5b02352.

[5] A. Banerjee, X. Wang, C. Fang, E. A. Wu, Y. S. Meng, Interfaces and interphases in all-solid-state batteries with inorganic solid electrolytes, Chem. Rev. 120 (14) (2020) 6878–6933. doi:10.1021/acs.chemrev.0c00101.

[6] S. A. Pervez, M. A. Cambaz, V. Thangadurai, M. Fichtner, Interface in solid-state lithium battery: Challenges, progress, and outlook, ACS Appl. Mater. Interfaces 11 (25) (2019) 22029–22050. doi:10.1021/acsami.9b02675.

[7] X. Chen, W. He, L.-X. Ding, S. Wang, H. Wang, Enhancing interfacial contact in all solid state batteries with a cathode-supported solid electrolyte membrane framework, Energy Environ. Sci. 12 (2019) 938–944. doi:10.1039/C8EE02617C.

[8] H.-K. Tian, Y. Qi, Simulation of the effect of contact area loss in all-solid-state Li-ion batteries, J. Electrochem. Soc. 164 (11) (2017) E3512–E3521. doi:10.1149/2.0481711jes.

[9] W. D. Richards, L. J. Miara, Y. Wang, J. C. Kim, G. Ceder, Interface stability in solid-state batteries, Chem. Mater. 28 (1) (2016) 266–273. doi:10.1021/acs.chemmater.5b04082.

[10] Y. Zhu, X. He, Y. Mo, First principles study on electrochemical and chemical stability of solid electrolyte–electrode interfaces in all-solid-state Li-ion batteries, J. Mater. Chem. A 4 (2016) 3253–3266. doi:10.1039/C5TA08574H.

[11] Y. Xiao, Y. Wang, S.-H. Bo, J. C. Kim, L. J. Miara, G. Ceder, Understanding interface stability in solid-state batteries, Nat. Rev. Mater. 5 (2) (2020) 105–126. doi:10.1038/s41578-019-0157-5.

[12] D. Santhanagopalan, D. Qian, T. McGilvray, Z. Wang, F. Wang, F. Camino, J. Graetz, N. Dudney, Y. S. Meng, Interface Limited Lithium Transport in Solid-State Batteries, J. Phys. Chem. Lett 5 (2) (2014) 298–303. doi:10.1021/jz402467x.

[13] K. H. Kim, Y. Iriyama, K. Yamamoto, S. Kumazaki, T. Asaka, K. Tanabe, C. A. Fisher, T. Hirayama, R. Murugan, Z. Ogumi, Characterization of the interface between $LiCoO_2$ and $Li_7La_3Zr_2O_{12}$ in an all-solid-state rechargeable lithium battery, J. Power Sources 196 (2) (2011) 764 – 767. doi:https://doi.org/10.1016/j.jpowsour.2010.07.073.

[14] F. S. Gittleson, F. El Gabaly, Non-Faradaic Li^+ migration and chemical coordination across solid-state battery interfaces, Nano Lett. 17 (11) (2017) 6974–6982. doi:10.1021/acs.nanolett.7b03498.

[15] N. J. J. de Klerk, M. Wagemaker, Space-charge layers in all-solid-state batteries; important or negligible?, ACS Appl. Energy Mater. 1 (10) (2018) 5609–5618. doi:10.1021/acsaem.8b01141.

[16] H. Masuda, N. Ishida, Y. Ogata, D. Ito, D. Fujita, Internal potential mapping of charged solid-state-lithium ion batteries using in situ Kelvin probe force microscopy, Nanoscale 9 (2017) 893–898. doi:10.1039/C6NR07971G.

[17] Y. Tian, T. Shi, W. D. Richards, J. Li, J. C. Kim, S.-H. Bo, G. Ceder, Compatibility issues between electrodes and electrolytes in solid-state batteries, Energy Environ. Sci. 10 (2017) 1150–1166. doi:10.1039/C7EE00534B.

[18] M. W. Swift, J. W. Swift, Y. Qi, Modeling the electrical double layer at solid-state electrochemical interfaces, Nat. Comput. Sci. 1 (3) (2021) 212–220. doi:10.1038/s43588-021-00041-y.

[19] L. Miara, A. Windmüller, C.-L. Tsai, W. D. Richards, Q. Ma, S. Uhlenbruck, O. Guillon, G. Ceder, About the compatibility between high voltage spinel cathode materials and solid oxide electrolytes as a function of temperature, ACS Appl. Mater. Interfaces 8 (40) (2016) 26842–26850. doi:10.1021/acsami.6b09059.

[20] M. Haruta, S. Shiraki, T. Suzuki, A. Kumatani, T. Ohsawa, Y. Takagi, R. Shimizu, T. Hitosugi, Negligible "negative space-charge layer effects" at oxide-electrolyte/electrode interfaces of thin-film batteries, Nano Letters 15 (3) (2015) 1498–1502. doi:10.1021/nl5035896.

[21] J. Li, C. Ma, M. Chi, C. Liang, N. J. Dudney, Solid electrolyte: the key for high-voltage lithium batteries, Adv. Energy Mater. 5 (4) (2015) 1401408. doi:https://doi.org/10.1002/aenm.201401408.

[22] C. Yada, A. Ohmori, K. Ide, H. Yamasaki, T. Kato, T. Saito, F. Sagane, Y. Iriyama, Dielectric modification of 5V class cathodes for high-voltage all-solid-state lithium batteries, Adv. Energy Mater. 4 (9) (2014) 1301416. doi:10.1002/aenm.201301416.

[23] F. Han, J. Yue, C. Chen, N. Zhao, X. Fan, Z. Ma, T. Gao, F. Wang, X. Guo, C. Wang, Interphase engineering enabled all-ceramic lithium battery, Joule 2 (3) (2018) 497–508. doi:https://doi.org/10.1016/j.joule.2018.02.007.

[24] Y.-S. Park, All-solid-state lithium thin-film rechargeable battery with lithium manganese oxide, Electrochem. Solid-State Lett. 2 (2) (1999) 58. doi:10.1149/1.1390733.

[25] Y. Iriyama, K. Nishimoto, C. Yada, T. Abe, Z. Ogumi, K. Kikuchi, Charge-transfer reaction at the lithium phosphorus oxynitride glass electrolyte/lithium manganese oxide thin-film interface and its stability on cycling, J. Electrochem Soc. 153 (5) (2006) A821. doi:10.1149/1.2178647.

[26] M. Fingerle, R. Buchheit, S. Sicolo, K. Albe, R. Hausbrand, Reaction and space charge layer formation at the $LiCoO_2$-LiPON interface: Insights on defect formation and ion energy level alignment by a combined surface science-

simulation approach, Chem. Mater. 29 (18) (2017) 7675–7685. doi:10.1021/acs.chemmater.7b00890.

[27] M. W. Swift, Y. Qi, First-principles prediction of potentials and space-charge layers in all-solid-state batteries, Phys. Rev. Lett. 122 (2019) 167701. doi:10.1103/PhysRevLett.122.167701.

[28] K. Yamamoto, Y. Iriyama, T. Asaka, T. Hirayama, H. Fujita, C. Fisher, K. Nonaka, Y. Sugita, Z. Ogumi, Dynamic Visualization of the Electric Potential in an All-Solid-State Rechargeable Lithium Battery, Angew. Chem. Int. Ed. 49 (26) (2010) 4414–4417. doi:10.1002/anie.200907319.

[29] T. Nakamura, K. Amezawa, J. Kulisch, W. G. Zeier, J. Janek, Guidelines for all-solid-state battery design and electrode buffer layers based on chemical potential profile calculation, ACS Appl. Mater. Interfaces 11 (22) (2019) 19968–19976. doi:10.1021/acsami.9b03053.

[30] Y. Aizawa, K. Yamamoto, T. Sato, H. Murata, R. Yoshida, C. A. Fisher, T. Kato, Y. Iriyama, T. Hirayama, In situ electron holography of electric potentials inside a solid-state electrolyte: Effect of electric-field leakage, Ultramicroscopy 178 (2017) 20–26. doi:https://doi.org/10.1016/j.ultramic.2016.07.015.

[31] S. Braun, C. Yada, A. Latz, Thermodynamically consistent model for space-charge-layer formation in a solid electrolyte, J. Phys. Chem. C 119 (39) (2015) 22281–22288. doi:10.1021/acs.jpcc.5b02679.

[32] E. J. Fuller, E. Strelcov, J. L. Weaver, M. W. Swift, J. D. Sugar, A. Kolmakov, N. Zhitenev, J. J. McClelland, Y. Qi, J. A. Dura, A. A. Talin, Spatially resolved potential and Li-ion distributions reveal performance-limiting regions in solid-state batteries, ACS Energy Letters 6 (2021) 3944–3951. doi:10.1021/acsenergylett.1c01960.

[33] J. Haruyama, K. Sodeyama, L. Han, K. Takada, Y. Tateyama, Space–Charge Layer Effect at Interface between Oxide Cathode and Sulfide Electrolyte in All-Solid-State Lithium-Ion Battery, Chem. Mater 26 (14) (2014) 4248–4255. doi:10.1021/cm5016959.

[34] B. Gao, R. Jalem, Y. Ma, Y. Tateyama, Li^+ transport mechanism at the heterogeneous cathode/solid electrolyte interface in an all-solid-state battery via the first-principles structure prediction scheme, Chem. Mater. 32 (1) (2020) 85–96. doi:10.1021/acs.chemmater.9b02311.

[35] K. Leung, A. J. Pearse, A. A. Talin, E. J. Fuller, G. W. Rubloff, N. A. Modine, Kinetics-controlled degradation reactions at crystalline LiPON/Li_xCoO_2 and crystalline LiPON/Li-metal interfaces, ChemSusChem 11 (12) (2018) 1956–1969. doi:10.1002/cssc.201800027.

[36] N. D. Lepley, N. A. W. Holzwarth, Modeling interfaces between solids: Application to Li battery materials, Phys. Rev. B 92 (2015) 214201. doi:10.1103/PhysRevB.92.214201.

[37] A. A. Delluva, J. Dudoff, G. Teeter, A. Holewinski, Cathode interface compatibility of amorphous $LiMn_2O_4$ (LMO) and $Li_7La_3Zr_2O_{12}$ (LLZO) characterized with thin-film solid-state electrochemical cells, ACS Appl. Mater Interfaces 12 (22) (2020) 24992–24999. doi:10.1021/acsami.0c03519.

[38] H. Kawasoko, S. Shiraki, T. Suzuki, R. Shimizu, T. Hitosugi, Extremely low resistance of Li_3PO_4 electrolyte/$Li(Ni_{0.5}Mn_{1.5})O_4$ electrode interfaces, ACS Appl. Mater. Interfaces 10 (32) (2018) 27498–27502. doi:10.1021/acsami.8b08506.

[39] M. Aykol, S. Kim, C. Wolverton, van der waals interactions in layered lithium cobalt oxides, J. Phys. Chem. C 119 (33) (2015) 19053–19058. doi:10.1021/acs.jpcc.5b06240.

[40] C. Freysoldt, B. Grabowski, T. Hickel, J. Neugebauer, G. Kresse, A. Janotti, C. G. Van de Walle, First-principles calculations for point defects in solids, Rev. Mod. Phys. 86 (2014) 253–305. doi:10.1103/RevModPhys.86.253.

[41] J. Pan, Y.-T. Cheng, Y. Qi, General method to predict voltage-dependent ionic conduction in a solid electrolyte coating on electrodes, Phys. Rev. B 91 (2015) 134116. doi:10.1103/PhysRevB.91.134116.

[42] D. Broberg, B. Medasani, N. E. Zimmermann, G. Yu, A. Canning, M. Haranczyk, M. Asta, G. Hautier, Pycdt: A python toolkit for modeling point defects in semiconductors and insulators, Comput. Phys. Commun 226 (2018) 165 – 179. doi:10.1016/j.cpc.2018.01.004.

[43] S. P. Ong, W. D. Richards, A. Jain, G. Hautier, M. Kocher, S. Cholia, D. Gunter, V. L. Chevrier, K. A. Persson, G. Ceder, Python materials genomics (pymatgen): A robust, open-source python library for materials analysis, Comput. Mater. Sci 68 (2013) 314 – 319. doi:0.1016/j.commatsci.2012.10.028.

[44] J. Bates, N. Dudney, G. Gruzalski, R. Zuhr, A. Choudhury, C. Luck, J. Robertson, Electrical properties of amorphous lithium electrolyte thin films, Solid State Ion. 53-56 (1992) 647–654. doi:https://doi.org/10.1016/0167-2738(92)90442-R.

[45] B. J. Neudecker, N. J. Dudney, J. B. Bates, "Lithium-free" thin-film battery with in situ plated Li anode, J. Electrochem. Soc. 147 (2) (2000) 517. doi:10.1149/1.1393226.

[46] K. Senevirathne, C. S. Day, M. D. Gross, A. Lachgar, N. Holzwarth, A new crystalline LiPON electrolyte: Synthesis, properties, and electronic structure, Solid State Ion. 233 (2013) 95 – 101. doi:10.1016/j.ssi.2012.12.013.

[47] A. J. Pearse, T. E. Schmitt, E. J. Fuller, F. El-Gabaly, C.-F. Lin, K. Gerasopoulos, A. C. Kozen, A. A. Talin, G. Rubloff, K. E. Gregorczyk, Nanoscale solid state batteries enabled by thermal atomic layer deposition of a lithium polyphosphazene solid state electrolyte, Chem. Mater. 29 (8) (2017) 3740–3753. doi:10.1021/acs.chemmater.7b00805.

[48] V. Lacivita, A. S. Westover, A. Kercher, N. D. Phillip, G. Yang, G. Veith, G. Ceder, N. J. Dudney, Resolving the amorphous structure of lithium phosphorus oxynitride (LiPON), J. Am. Chem. Soc. 140 (35) (2018) 11029–11038. doi:10.1021/jacs.8b05192.

[49] N. D. Lepley, N. A. W. Holzwarth, Y. A. Du, Structures, Li^+ mobilities, and interfacial properties of solid electrolytes Li_3PS_4 and Li_3PO_4 from first principles, Phys. Rev. B 88 (2013) 104103. doi:10.1103/PhysRevB.88.104103.

[50] R. Murugan, V. Thangadurai, W. Weppner, Fast lithium ion conduction in garnet-type $Li_7La_3Zr_2O_{12}$, Angew. Chem. Int. Ed 46 (41) (2007) 7778–7781. doi:10.1002/anie.200701144.

[51] N. Bernstein, M. D. Johannes, K. Hoang, Origin of the structural phase transition in $Li_7La_3Zr_2O_{12}$, Phys. Rev. Lett. 109 (2012) 205702. doi:10.1103/PhysRevLett.109.205702.

[52] Y. Wang, W. D. Richards, S. P. Ong, L. J. Miara, J. C. Kim, Y. Mo, G. Ceder, Design principles for solid-state lithium superionic conductors, Nat. Mater. 14 (10) (2015) 1026–1031.

[53] Y. Ren, Y. Shen, Y. Lin, C.-W. Nan, Direct observation of lithium dendrites inside garnet-type lithium-ion solid electrolyte, Electrochemistry Communications 57 (2015) 27–30. doi:https://doi.org/10.1016/j.elecom.2015.05.001.

[54] L. Wang, B. Chen, J. Ma, G. Cui, L. Chen, Reviving lithium cobalt oxide-based lithium secondary batteries-toward a higher energy density, Chem. Soc. Rev. 47 (2018) 6505–6602. doi:10.1039/C8CS00322J.

[55] K. Mizushima, P. Jones, P. Wiseman, J. Goodenough, Li_xCoO_2 ($0 < x < 1$): A new cathode material for batteries of high energy density, Mater. Res. Bull. 15 (6) (1980) 783–789. doi:https://doi.org/10.1016/0025-5408(80)90012-4.

[56] P. Kalyani, N. Kalaiselvi, Various aspects of $LiNiO_2$ chemistry: A review, Sci. Technol. Adv. Mater. 6 (6) (2005) 689–703. doi:10.1016/j.stam.2005.06.001.

[57] J. Dahn, U. von Sacken, C. Michal, Structure and electro-

chemistry of $Li_{1\pm y}NiO_2$ and a new Li_2NiO_2 phase with the $Ni(OH)_2$ structure, Solid State Ion. 44 (1) (1990) 87–97. doi:https://doi.org/10.1016/0167-2738(90)90049-W.

[58] W. Liu, P. Oh, X. Liu, M.-J. Lee, W. Cho, S. Chae, Y. Kim, J. Cho, Nickel-rich layered lithium transition-metal oxide for high-energy lithium-ion batteries, Angew. Chem. Int. Ed. 54 (15) (2015) 4440–4457. doi:https://doi.org/10.1002/anie.201409262.

[59] F. Marchini, S. Saha, D. Alves Dalla Corte, J. M. Tarascon, Li-rich layered sulfide as cathode active materials in all-solid-state Li–metal batteries, ACS Appl. Mater. Interfaces 12 (13) (2020) 15145–15154. doi:10.1021/acsami.9b22937.

[60] C. Chen, J. Liu, M. Stoll, G. Henriksen, D. Vissers, K. Amine, Aluminum-doped lithium nickel cobalt oxide electrodes for high-power lithium-ion batteries, J. Power Sources 128 (2) (2004) 278–285. doi:https://doi.org/10.1016/j.jpowsour.2003.10.009.

[61] S. Sivaprakash, S. Majumder, S. Nieto, R. Katiyar, Crystal chemistry modification of lithium nickel cobalt oxide cathodes for lithium ion rechargeable batteries, J. Power Sources 170 (2) (2007) 433–440. doi:https://doi.org/10.1016/j.jpowsour.2007.04.029.

[62] M. Thackeray, P. Johnson, L. de Picciotto, P. Bruce, J. Goodenough, Electrochemical extraction of lithium from $LiMn_2O_4$, Mater. Res. Bull. 19 (2) (1984) 179–187. doi:https://doi.org/10.1016/0025-5408(84)90088-6.

[63] G. Liang, V. K. Peterson, K. W. See, Z. Guo, W. K. Pang, Developing high-voltage spinel $LiNi_{0.5}Mn_{1.5}O_4$ cathodes for high-energy-density lithium-ion batteries: current achievements and future prospects, J. Mater. Chem. A 8 (2020) 15373–15398. doi:10.1039/D0TA02812F.

[64] W. Li, H. Y. Asl, Q. Xie, A. Manthiram, Collapse of $LiNi_{1-x-y}Co_xMn_yO_2$ lattice at deep charge irrespective of nickel content in lithium-ion batteries, J. Am. Chem. Soc. 141 (13) (2019) 5097–5101. doi:10.1021/jacs.8b13798.

[65] Y. Bi, J. Tao, Y. Wu, L. Li, Y. Xu, E. Hu, B. Wu, J. Hu, C. Wang, J.-G. Zhang, Y. Qi, J. Xiao, Reversible planar gliding and microcracking in a single-crystalline ni-rich cathode, Science 370 (6522) (2020) 1313–1317. doi:10.1126/science.abc3167.

[66] S. Shiraki, T. Shirasawa, T. Suzuki, H. Kawasoko, R. Shimizu, T. Hitosugi, Atomically well-ordered structure at solid electrolyte and electrode interface reduces the interfacial resistance, ACS Appl. Mater. Interfaces 10 (48) (2018) 41732–41737. doi:10.1021/acsami.8b08926.

[67] C. Vinado, S. Wang, Y. He, X. Xiao, Y. Li, C. Wang, J. Yang, Electrochemical and interfacial behavior of all solid state batteries using $Li_{10}SnP_2S_{12}$ solid electrolyte, J. Power Sources 396 (2018) 824–830. doi:https://doi.org/10.1016/j.jpowsour.2018.06.038.

[68] X. Li, Q. Sun, Z. Wang, D. Song, H. Zhang, X. Shi, C. Li, L. Zhang, L. Zhu, Outstanding electrochemical performances of the all-solid-state lithium battery using Ni-rich layered oxide cathode and sulfide electrolyte, J. Power Sources 456 (2020) 227997. doi:https://doi.org/10.1016/j.jpowsour.2020.227997.

[69] A.-Y. Kim, F. Strauss, T. Bartsch, J. H. Teo, T. Hatsukade, A. Mazilkin, J. Janek, P. Hartmann, T. Brezesinski, Stabilizing effect of a hybrid surface coating on a Ni-rich NCM cathode material in all-solid-state batteries, Chem. Mater. 31 (23) (2019) 9664–9672. doi:10.1021/acs.chemmater.9b02947.

[70] Z. Bi, N. Zhao, L. Ma, C. Shi, Z. Fu, F. Xu, X. Guo, Surface coating of $LiMn_2O_4$ cathodes with garnet electrolytes for improving cycling stability of solid lithium batteries, J. Mater. Chem. A 8 (2020) 4252–4256. doi:10.1039/C9TA11203K.

[71] A. Kato, H. Kowada, M. Deguchi, C. Hotehama, A. Hayashi, M. Tatsumisago, XPS and SEM analysis between Li/Li_3PS_4 interface with Au thin film for all-solid-state lithium batteries, Solid State Ion. 322 (2018) 1–4. doi:https://doi.org/10.1016/j.ssi.2018.04.011.

[72] F. Han, A. S. Westover, J. Yue, X. Fan, F. Wang, M. Chi, D. N. Leonard, N. J. Dudney, H. Wang, C. Wang, High electronic conductivity as the origin of lithium dendrite formation within solid electrolytes, Nat. Energy 4 (3) (2019) 187–196. doi:10.1038/s41560-018-0312-z.

[73] T. Thompson, S. Yu, L. Williams, R. D. Schmidt, R. Garcia-Mendez, J. Wolfenstine, J. L. Allen, E. Kioupakis, D. J. Siegel, J. Sakamoto, Electrochemical window of the Li-ion solid electrolyte $Li_7La_3Zr_2O_{12}$, ACS Energy Lett. 2 (2) (2017) 462–468. doi:10.1021/acsenergylett.6b00593.

[74] H.-K. Tian, B. Xu, Y. Qi, Computational study of lithium nucleation tendency in $Li_7La_3Zr_2O_{12}$ (LLZO) and rational design of interlayer materials to prevent lithium dendrites, J. Power Sources 392 (2018) 79 – 86. doi:https://doi.org/10.1016/j.jpowsour.2018.04.098.

[75] H.-K. Tian, Z. Liu, Y. Ji, L.-Q. Chen, Y. Qi, Interfacial electronic properties dictate li dendrite growth in solid electrolytes, Chemistry of Materials 31 (18) (2019) 7351–7359. doi:10.1021/acs.chemmater.9b01967.

[76] S. P. Ong, L. Wang, B. Kang, G. Ceder, Li-Fe-P-O2 Phase Diagram from First Principles Calculations, Chem. Mater. 20 (5) (2008) 1798–1807. doi:10.1021/cm702327g.

[77] A. Jain, S. P. Ong, G. Hautier, W. Chen, W. D. Richards, S. Dacek, S. Cholia, D. Gunter, D. Skinner, G. Ceder, K. A. Persson, Commentary: The materials project: A materials genome approach to accelerating materials innovation, APL Mater. 1 (1) (2013) 011002. doi:10.1063/1.4812323.

[78] S. Braun, C. Yada, A. Latz, Thermodynamically consistent model for space-charge-layer formation in a solid electrolyte, J. Phys. Chem. C 119 (39) (2015) 22281–22288. doi:10.1021/acs.jpcc.5b02679.

[79] W. Weppner, R. A. Huggins, Determination of the kinetic parameters of mixed-conducting electrodes and application to the system Li_3Sb, J. Electrochem. Soc. 124 (10) (1977) 1569–1578. doi:10.1149/1.2133112.

[80] X. Li, Q. Sun, Z. Wang, D. Song, H. Zhang, X. Shi, C. Li, L. Zhang, L. Zhu, Outstanding electrochemical performances of the all-solid-state lithium battery using ni-rich layered oxide cathode and sulfide electrolyte, J. Power Sources 456 (2020) 227997. doi:https://doi.org/10.1016/j.jpowsour.2020.227997.